

Seepage-induced penetration of water vapor and dust beneath ripples and dunes

M. Y. Louge,¹ A. Valance,² H. Mint Babah,² J.-C. Moreau-Trouvé,³ A. Ould el-Moctar,⁴ P. Dupont⁵ and D. Ould Ahmedou,⁶

Abstract. We present stratigraphic measurements of humidity and bulk density beneath the surface of a barchan dune obtained with a capacitance probe. A model shows that air seeping through the sand bed in response to spatial variations of static pressure along the ripple surface guides water vapor through ripple crests and gradually stores dust beneath troughs. The accumulated dust remains trapped beneath the relatively compact trough surface until wind is violent enough to mobilize sand deeply.

1. Introduction

Sand dunes are ubiquitous features of the desert. Their growth, morphology and travel are governed by wind-driven granular transport. Their shape determines overall characteristics of the particle-laden flow, such as acceleration on an upwind-facing slope, flow separation and recirculation downstream [Livingstone *et al.*, 2007].

If an inexhaustible sand source lies upstream of a vast expanse featuring a hard, flat base, and if a wind direction prevails, individual barchan dunes form. Such dunes only endure if their scale exceeds the “transport saturation length” [Sauermaun *et al.*, 2001; Andreotti *et al.*, 2008]. Sand piles of smaller dimensions erode away, quickly forming thin, fast-moving streamwise strands transporting solids to the next dune. On the upwind toe of a barchan, the “saltation” process progressively raises the concentration of the particle cloud [Rasmussen *et al.*, 1996]. On a long enough dune, concentration increases until it reaches a value beyond which turbulence no longer musters enough fluctuation kinetic energy to keep grains aloft. In this case, grains settle again on the same dune, thus sustaining its existence. In contrast, short dunes disappear if the particle cloud overhead is too dilute to saturate the turbulent kinetic energy [Andreotti *et al.*, 2002].

Numerical models provide insight on the large-scale flow around barchans [Schuämmle and Herrmann, 2005; Parsons *et al.*, 2004]. The gentle stoss face of a barchan is interrupted by a brink behind which the flow recirculates downward and inward. In its wake, suspended sand loses momentum and accumulates onto the steep slope. Because intermittent avalanches maintain the slope at its angle of repose by rapidly transferring excess grains downward, the rate of dune migration is limited by the relatively slower wind-driven granular transport on the dune’s stoss face. Sand involved in avalanches is trapped. The lee face of the

barchan dune is terminated by horns revealing the formation of “wing vortices” on either side and giving the dune its crescent shape. Sand escaping to the next barchan originates from these horns [Hersen, 2004].

Particles trapped in barchan dunes typically possess a narrow size distribution with mean diameter $d \sim 200\mu\text{m}$. Wind mobilizes them as a “reptation” shear layer on the bed surface, and a more dilute, faster-moving “saltation” region above [Andreotti, 2004]. Variations of the reptation mass flow rate along the wind direction x create a shifting pattern of ripples with crest line perpendicular to x [Bagnold, 1935; Csahók *et al.*, 2000] and wavelength increasing linearly with wind speed [Andreotti *et al.*, 2006]. In a companion paper [Louge *et al.*, 2009], we showed that the bulk density along the surface of a dry sand ripple at rest varies from the random jammed packing at troughs to the minimum value for a stable packing at crests. We also noted that the evolution of static pressure at the ripple surface induces a “seepage” flow within the sand bed. In Appendix A, we summarize a model of seepage. This mechanism is similar to advective pore-water flow in nearshore permeable sediments, which Meysman *et al.* [2007] analyzed, and which leads, for example, to the filtration of planktonic algal cells [Huettel *et al.*, 2007] or to benthic solute exchange [Cook *et al.*, 2007] through underwater ripples.

In this paper, we discuss consequences of seepage on the penetration of moisture and dust through the dune surface. To inform this process, we report stratigraphic measurements of bulk density and water mass fraction on a barchan. Because the local seepage flow rate decays exponentially from the surface on a scale about one sixth of the ripple wavelength ($1/2\pi$), we focus on a region just beneath ripples, unlike the deeper excavations of McKee [1979] or the stratigraphy of Bristow *et al.* [2000] using ground-penetrating-radar. Exploiting the simple advection model in Appendix A, we show that seepage guides the transfer of water vapor preferentially through ripple crests, and accumulates fine particles below troughs.

We begin by describing a new capacitance instrument that records bulk density and adsorbed water mass fraction versus depth. We then report stratigraphic data of bulk density and humidity at selected points on a test barchan near Akjoujt, Mauritania. Finally, we present models for the transfer of water vapor and dust through the surface.

2. Instruments

To record stratigraphic profiles of humidity and bulk density in the dune, we exploited the portable capacitance probe that Louge *et al.* [1997, 1998] developed for measuring dielectric properties of the snow pack. As Figure 1 shows, we

¹Sibley School of Mechanical and Aerospace Engineering, Cornell University, Ithaca, NY 14853, USA.

²Institut de Physique de Rennes, Université de Rennes 1, France.

³Lycée Victor Hugo, Hennebont, France.

⁴Ecole Polytechnique de l’Université de Nantes, France.

⁵Institut National des Sciences Appliquées de Rennes, France.

⁶Université de Nouakchott, République Islamique de Mauritanie.

mounted the probe at the end of a rigid aluminum bar penetrating the first 30cm of the dune. The geometry of its conductive surfaces, its nominal capacitance in air $C_0 \simeq 25$ fF, and its principle of operation are identical to those of the ripple probe described in our companion paper [Louge *et al.*, 2009]. Its measurement volume is thin in the vertical direction $\simeq 3.1$ mm, thus permitting detailed stratigraphic

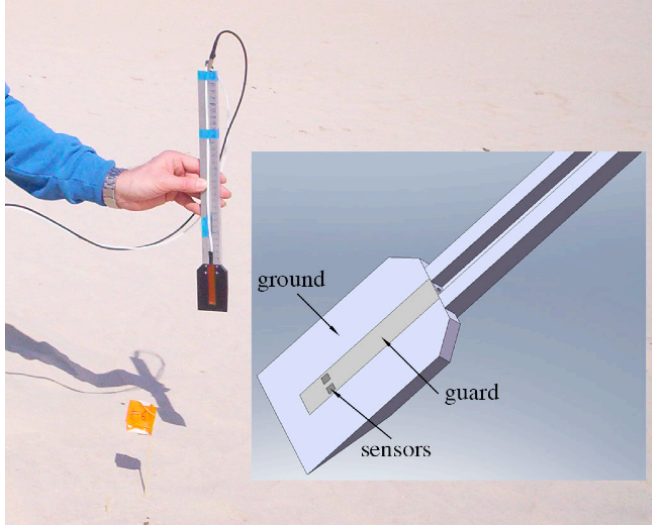


Figure 1. Stratigraphic probe held by a metal bar maintained at the reference voltage (“ground”) and graduated to identify depth. The processing electronics records impedance between sensor and ground; the guard surrounds the sensor to eliminate stray and cable capacitances [Louge *et al.*, 2009].

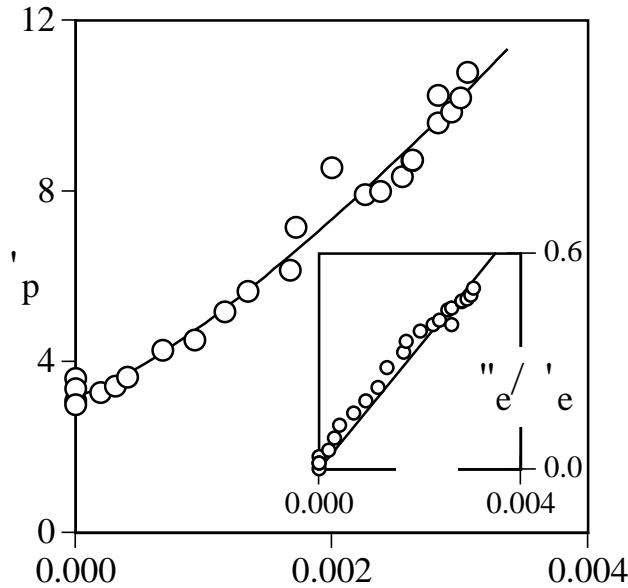


Figure 2. Real part of the material dielectric constant vs. water mass fraction adsorbed on sand. Symbols are data and the line is $\epsilon'_p = 3.2 + (1500\Omega)^{1.3}$. Inset: “loss tangent” ϵ''_e/ϵ'_e vs. Ω for samples with $0.67 < \nu < 0.69$. The line is $\epsilon''_e/\epsilon'_e = \Omega/\Omega_0$ with $\Omega_0 \simeq 0.0058$.

records, while extending $\simeq 11$ mm away from the probe in the horizontal direction.

Like snow, humid sand possesses a complex dielectric constant

$$\epsilon_e = \epsilon'_e - i\epsilon''_e, \quad (1)$$

where $i^2 = -1$; the real and imaginary parts $\epsilon'_e(\nu; \Omega)$ and $\epsilon''_e(\nu; \Omega)$ are functions of the solid volume fraction ν and the fraction Ω of the total bed mass that is composed of water. Ignoring air mass, the solid volume fraction $\nu = \rho_b/\rho_s$ is the ratio of bulk density ρ_b and sand material density ρ_s . Its complement $(1 - \nu)$ is the “voidage”. Ω is related to the “volumetric water content” $\theta \approx \rho_s\Omega\nu/\rho_w$, where ρ_w is the density of liquid water.

As Louge *et al.* [2009] outlined, the portable, self-contained electronics that we used (Capacitex model 4100 with PC-201 preamplifier) recorded a 15kHz signal from which ϵ_e could be calculated. Following the suggestions of Louge *et al.* [1997] for non-spherical particles, we adopted the homogenization model of Böttcher [1952] to describe the dependence of the real part of the effective dielectric constant on ν ,

$$\frac{\epsilon'_e(\nu; \Omega) - 1}{3\epsilon'_e(\nu; \Omega)} = \nu \frac{\epsilon'_p(\Omega) - 1}{\epsilon'_p(\Omega) + 2\epsilon'_e(\nu; \Omega)}. \quad (2)$$

In general, $\epsilon'_p(\Omega)$ represents the real part of the material dielectric constant of the grains, including adsorbed water. To interpret stratigraphic data with humid sand, we carried out calibrations in a laboratory glovebox filled with nitrogen at known relative humidities. We dried the sample at 40°C under vacuum to infer Ω from its change of mass, and we

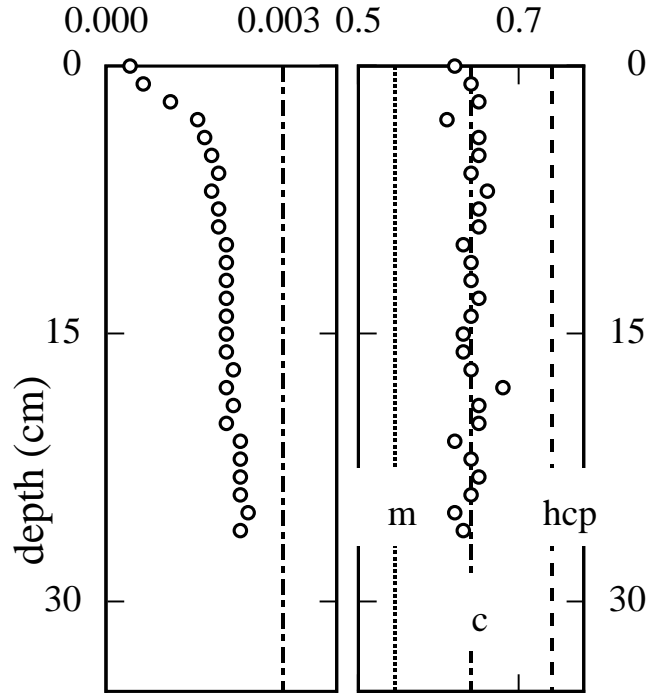


Figure 3. Typical stratigraphy taken at point 13. Vertical axis: depth in cm. The left graph shows ϵ'_p ; its vertical line marks the largest $\Omega_{\text{max}} \simeq 0.003$ recordable with this pre-amplifier without instabilities. The right graph is ν ; its vertical lines are $\nu = \nu_m \simeq 0.545$, $\nu = \nu_c \simeq 0.64$ and the hexagonal close packing of spheres $\nu = \nu_{\text{hcp}} = \pi/3\sqrt{2}$.

calculated ϵ'_p from the measured ϵ_e and ν using equation (2). Figure 2 shows how ϵ'_p varies with Ω . It also reveals that the “loss tangent” i.e., the ratio ϵ''/ϵ'_e , varies linearly with moisture content, $\epsilon''/\epsilon'_e = \Omega/\Omega_0$. By progressively compacting samples on a shake table, we also established that Ω_0 is insensitive to volume fraction in the range $0.59 < \nu < 0.69$. Thus, assuming that Ω_0 does not change with ν , we reduced our field data of ϵ_e by inferring Ω from ϵ''/ϵ'_e and, from the corresponding value of $\epsilon'_p(\Omega)$ in Figure 2, we calculated ν from equation (2). (While this assumption is reasonable at

the low Ω and high ν of interest here, it may be suspect with systems simultaneously having wider excursions in ν and greater Ω .)

As *Louge et al.* [1998] showed with snow, the probe, although invasive, hardly disturbs ν in front of its sensors as it penetrates sand, thanks to a sharp 10° taper that transmits stresses mostly behind it, and to a narrow cross section of only 4 mm thickness at the sensors. The probe’s ability to detect subtle density variations in snow and sand suggests that its intrusiveness is indeed minimal.

3. Measurements

3.1. Stratigraphy

We recorded vertical profiles of Ω and ν on a barchan dune at the site studied by *Ould Ahmedou et al.* [2007] near Akjoujt, Mauritania, at $19^\circ 50.666' N$, $14^\circ 08.842' W$ on December 16, 2006. Figure 3 shows a typical result for water mass fraction (left) and solid volume fraction (right). Because prevailing winds shifted to the South-East shortly before the campaign, the dune was not perfectly symmetric. Nonetheless, it included all zones identified by *Wiggs et al.* [1996]; starting downwind, it featured a horn (points 1 to 3; Figure 4), a convex “zone C” from brink to summit (points 4 to 6; Figures 4-5), a convex “zone B” upwind from the summit (points 7 to 12; Figures 5-7), and a concave “zone A” windward (points 13 and 14; Figure 7).

Although the bed mostly possessed a volume fraction near random jammed packing $\nu_c \simeq 0.64$ [*Torquato*, 1995], we distinguished a layered internal structure most evident at points 9 and 10 near the summit, beneath which grains were recently deposited. This pattern may be part of deeper strata marking past positions of the avalanche face. At point 3, we observed a relatively low volume fraction near the surface to a depth of approximately 5 cm, indicating the recent buildup of loose material on the surface.

The greatest contrast among different zones was in the moisture profiles. As Figure 8 shows, humidity was relatively high beneath the windward side (points 11 to 14). It increased from the surface on a length scale of approximately 3 cm, a distance much smaller than the depth $\sim \sqrt{D J / \pi} \simeq 0.4$ m through which water vapor is transferred in and out of the bed on the diurnal period $J = 24 \times 3600$ s

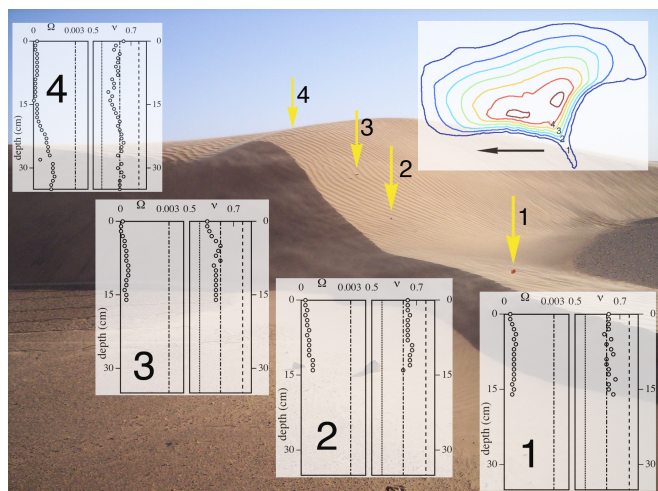


Figure 4. Points 1 to 3 along the horn and point 4 in zone C. Each graph of Ω (left) and ν (right) has similar axes than Figure 3. Contour map and arrows in the background mark where data were recorded. Elevation contours are every 0.5 m. The black arrow points North and is 10 m long.

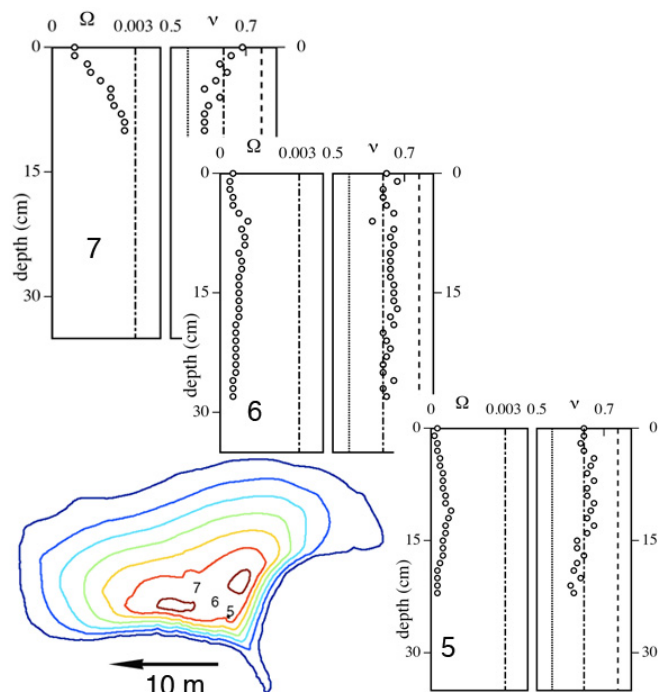


Figure 5. Points 5 and 6 (zone C) and point 7 (zone B); symbols and scales, see Figures 3 and 4.

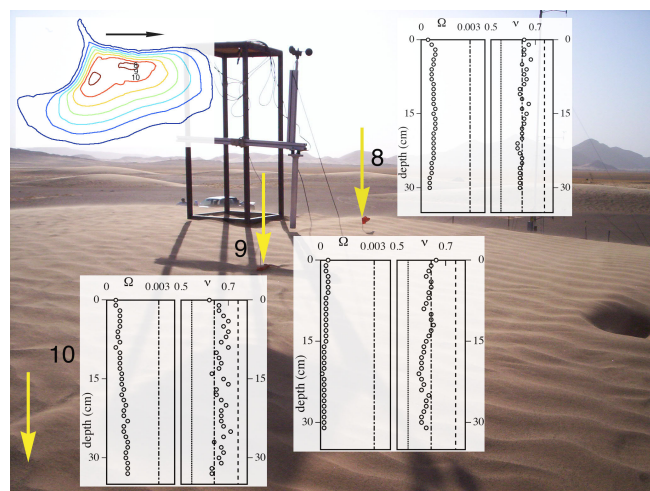


Figure 6. Point 8 (transition B1), and points 9 and 10 (zone B) near the summit; symbols and scales, see Figures 3 and 4. A *post-facto* excavation revealed no noticeably cohesive material beneath the surface.

at the diffusion coefficient \mathcal{D} [Carslaw and Jaeger, 1959]. However, because it coincided with the characteristic seepage depth $L/(2\pi) \sim 2.5$ cm that we calculate in Appendix A from the ripple wavelength L , seepage seemed to play an important role in the water vapor exchange near the surface.

In contrast, although some moisture appeared trapped deep beneath point 4 and exhibited a local maximum below points 1, 3, 4, 5 and 6, humidity was low or non-existent beneath the brink, the horns and the avalanching face. We observed no noticeably cohesive sand material below the surface at points 7-10 in zone B, or in the horns (Figs. 5 and 6).

Excavations below windward points 12-14 uncovered a subsurface “mantle” of greater cohesion. Coincidentally, this windward region of trapped moisture also featured large, long-lasting “giant” ripples [Manukyan and Prigozhin, 2009]. As the particle size distributions (PSD) in Figure 8 suggest, these ripples endured because a few coarser, denser dark grains, likely containing pyroxene, magnetite and olivine, accumulated on their crests. We exploited the unusual perennial character of these larger ripples to observe patterns of moisture transfer underneath. In particular, the bottom photograph of Figure 7 shows a vertical accretion of sand material rising below a crest at point 14, and a

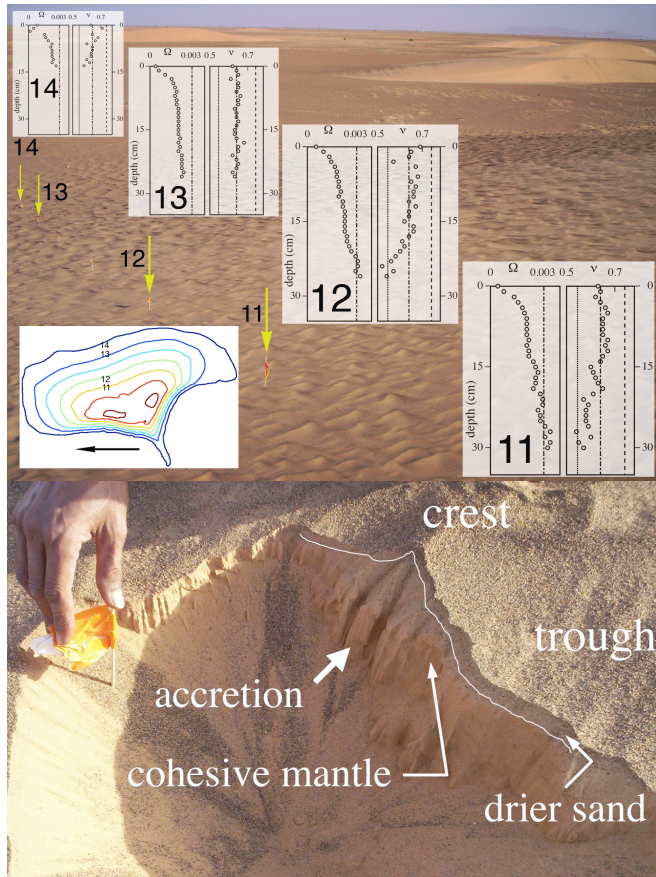


Figure 7. Top: stratigraphy at points 11 and 12 in convex zone B, and at points 13 and 14 in concave zone A. Bottom: excavation near point 14. The line marks the boundary between a buried cohesive “mantle” and a drier, cohesionless sand layer near the surface. Beneath the trough, this cohesionless surface layer is ~ 2 cm thick. The arrow marks a vertical accretion of cohesive material rising just beneath the crest, suggesting the channeling of moisture there.

drier, cohesionless sand layer that is thickest below troughs. We observed a similar pattern near point 12. As theory in the next section suggests, the accretion is consistent with the channeling of moisture through crests, and the thick, relatively dense cohesionless base implies that dry ambient conditions prevail below troughs.

4. Models

In this section, we calculate how the seepage flow described in Appendix A guides water vapor through crests and accumulates dust beneath troughs.

4.1. Moisture transfer

Any water vapor imbalance between sand bed and ambient air drives a net flux of humidity through the surface. In this process, seepage plays a significant role in channeling vapor transfer through ripple crests. To illustrate this, we solve the steady mass balance $\mathbf{v} \cdot \nabla \Psi = \mathcal{D} \nabla^2 \Psi$ in the porous bed, where $\mathcal{D}(\nu)$ is the diffusion coefficient of water vapor in air through the bed of volume fraction ν , $\mathbf{v} \equiv \mathbf{u}/(1-\nu)$ is the interstitial gas velocity, \mathbf{u} is the superficial gas velocity, and Ψ is the mass fraction of water vapor in air. For simplicity, we use the homogenization model of Maxwell [1892] to relate $\mathcal{D} = 2\mathcal{D}_0(1-\nu)/(2+\nu)$ to the molecular diffusion coefficient without solids, $\mathcal{D}_0 \equiv \mathcal{D}(\nu = 0)$. At small relative humidity RH, $\Psi \simeq (MW_{H_2O}/MW_{air})(p_{H_2O,sat}/p)RH$, where MW is molecular weight, $p_{H_2O,sat}$ is the partial pressure of water vapor in air, and p is ambient pressure. We assume that the mass fraction Ψ of water vapor in air is at equilibrium with its counterpart Ω adsorbed on grains, so there is no net exchange of water between grains and humid interstitial air at steady-state. Because mass transfer through the bed is slower than through the turbulent boundary layer atop, these two processes operate in series, their rate is limited by mass transfer in the bed, and $\Psi(y^\dagger = 0)$ is the value Ψ_0 in the ambient.

If the bed resides on a horizontal surface at $y = \ell_i$ blocking seepage, but serving as a reservoir of constant mass fraction Ψ_ℓ , we introduce the relative variable $\Psi^\dagger \equiv (\Psi - \Psi_0)/(\Psi_\ell - \Psi_0)$. If instead the bed is boundless, we

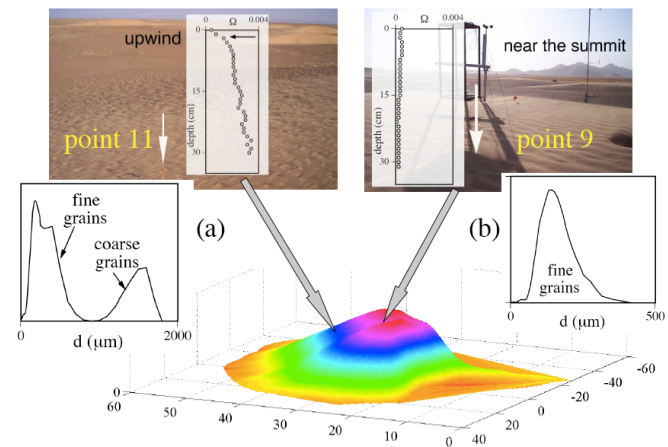


Figure 8. Composite graph contrasting depth profiles of humidity at (a) point 9 near the summit and (b) point 11 upwind, and showing size distribution vs. grain diameter (μm) of particles collected at those points, normalized as $\int_{d=0}^{\infty} \text{PSD}(\xi) d\xi \equiv 1$. The false-color elevation map shows dune topography with exaggerated vertical scale. The horizontal arrow marks the top of the cohesive “mantle” revealed in Figure 7.

solve the governing equations subject to a constant net water vapor flux $\Sigma \cdot \hat{\mathbf{y}} \equiv \Sigma_\infty$ deep in the dune and define $\Psi^\dagger \equiv (\Psi - \Psi_0)/\Sigma_\infty$. In general, the net water vapor flux is $\Sigma = \rho\Psi\mathbf{v} - \rho\mathcal{D}\nabla\Psi$. We then write the mass balance in dimensionless form

$$\mathbf{u}^\dagger \cdot \nabla^\dagger \Psi^\dagger = \mathcal{D}^\dagger \left[\frac{\partial^2 \Psi^\dagger}{\partial x^{\dagger 2}} + \frac{\partial^2 \Psi^\dagger}{\partial y^{\dagger 2}} \right], \quad (3)$$

where \mathbf{u}^\dagger is the dimensionless seepage velocity vector given by equation (A7) if ℓ_i is finite or by equation (A6) if it is not. Dimensionless quantities denoted by a dagger[†]. Coordinates and lengths are made dimensionless with the ripple wavelength. The relative diffusion coefficient is

$$\mathcal{D}^\dagger \equiv \frac{150}{\pi} \frac{\nu^2}{(1-\nu)(2+\nu)} \frac{\eta}{(h_0/L)} \frac{\mu\mathcal{D}_0}{\rho U^2 d^2}, \quad (4)$$

where U is wind speed, μ and ρ are gas viscosity and density, respectively, h_0 is ripple amplitude, and $\eta \simeq 0.14$ is inferred from the data of *Gong et al.* [1996]. Because equation (3) has no analytical solution, we solve it with COMSOL MULTIPHYSICS subject to $\Psi^\dagger = 0$ at the surface ($y^\dagger = 0$), and, by symmetry, $\partial\Psi^\dagger/\partial x^\dagger = 0$ at $x^\dagger = 0, 1$. Although it is best to solve the convection-diffusion equation using a flux-conserving finite-difference approximation, this convenient commercial finite-element software works well with the linear problem of interest here. For a finite bed, we impose $\Psi^\dagger = 1$ at $y^\dagger = \ell_i^\dagger$. For a boundless bed, we set the flux magnitude $\Sigma = \Sigma_\infty$ as $y^\dagger \rightarrow \infty$. We refine the mesh and extend the boundary along y^\dagger until input and output fluxes are balanced, and the solution is insensitive to further changes.

Figure 9 illustrates the results for a boundless bed with two values of \mathcal{D}^\dagger . Its lower graphs show contours of Ψ^\dagger

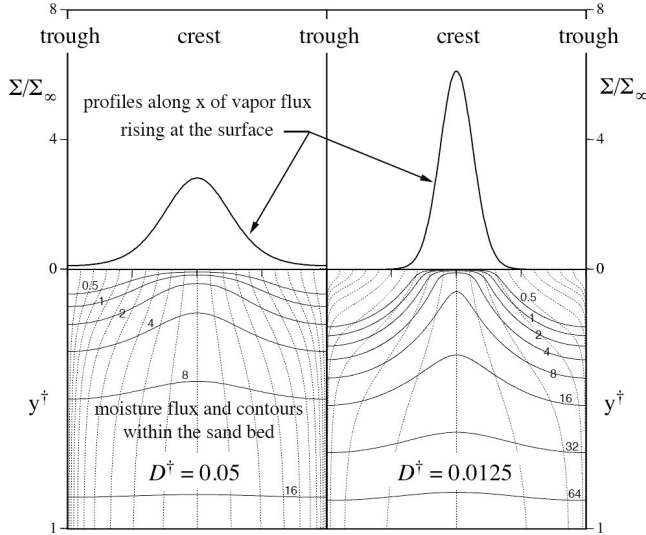


Figure 9. Bottom graphs: mass transfer beneath a ripple without an impermeable barrier ($\ell_i \rightarrow \infty$); solid curves: contours, from top to bottom, of $(\Psi - \Psi_0)/\Sigma_\infty = 0.5, 1, 2, 4, 8, 16, 32$ and 48 ; dotted curves are moisture flux lines. Top graphs: profiles along x of vapor flux emerging at the surface. Conditions are $\mathcal{D}^\dagger = 0.05$ (left graphs) and 0.0125 (right graphs); they correspond, for example, to $150 \mu\text{m}$ spherical sand grains with humid air ($\mathcal{D}_0 = 2.6 \cdot 10^{-5} \text{ m}^2/\text{s}$) in a bed at $\nu = \nu_c$, featuring ripples with $h_0/L = 0.02$ inducing a surface profile of static pressure (equation A1) with $\eta \simeq 0.14$ at winds speeds of $U \simeq 7$ and 14 m/s , respectively.

and lines of net flux within the bed between two consecutive troughs. The upper graphs plot the net relative water vapor flux Σ/Σ_∞ inhaled ($\Psi_0 > \Psi_\infty, \Sigma_\infty > 0$) or exhaled ($\Psi_0 < \Psi_\infty, \Sigma_\infty < 0$) through the surface. In general, the relative flux is always greater at crests. For $\mathcal{D}^\dagger = 0.05$ (left graphs), troughs exhibit a finite water vapor flux $\Sigma/\Sigma_\infty \neq 0$. However, for $\mathcal{D}^\dagger = 0.0125$ (right graphs), seepage is intense enough to create a region beneath troughs that is completely permeated with ambient conditions, such that $\Sigma(y^\dagger = 0)/\Sigma_\infty$ vanishes there. Surface fluxes vanish at troughs for any $\mathcal{D}^\dagger \lesssim 0.025$.

Therefore, seepage causes troughs to adopt dry ambient conditions more readily, as the excavations shown in

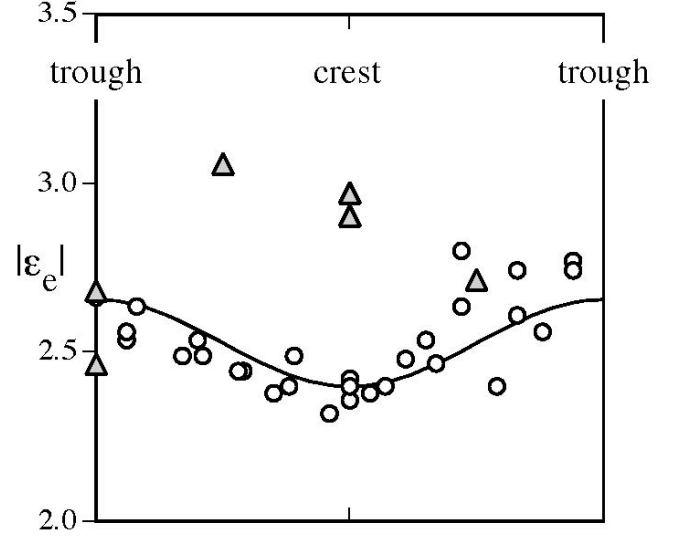


Figure 10. Effective dielectric modulus along a ripple with moderate winds blowing from the left. Circles are data on a dry substrate in zone C; the line is a sine fit. Triangles are from a humid base in zone A; consistent with predictions of our model, higher values of $|\epsilon_e|$ suggest channeling of water vapor through crests.

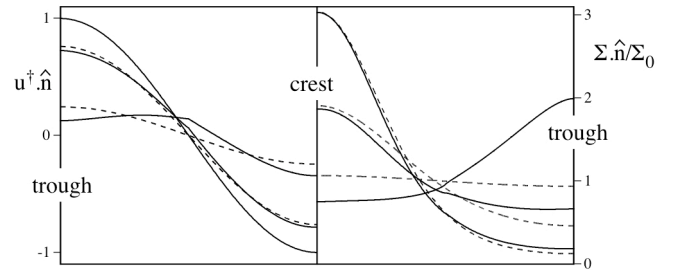


Figure 11. Profile of seepage velocity $\mathbf{u}^\dagger \cdot \hat{\mathbf{n}}$ (left graph) and mass flux $\Sigma \cdot \hat{\mathbf{n}}$ relative to its counterpart Σ_0 without seepage (right graph) at the bed surface ($y^\dagger = 0$) along the normal $\hat{\mathbf{n}}$ directed *into* the bed from trough ($x^\dagger = 0$) to crest ($x^\dagger = 1/2$) for $h_0/L = 0.02$, $\mathcal{D}^\dagger = 0.05$ and $\Psi_0 = 0$. Left curves represent, from top to bottom at the trough, a seepage barrier located at a depth $y = L, L/(2\pi)$ and $L/(8\pi)$. Right curves share the same series of depths from top to bottom at the crest. Solid lines are numerical results with the actual wavy ripple surface; dashed lines are predictions assuming a flat bed surface.

Figure 7 suggested. Conversely, humidity passes mainly through crests. This mechanism explains why we recorded greater $|\epsilon_e|$ at crests than troughs at dune locations with a more humid substrate, like points 11-14 (Figure 10).

Figure 11 illustrates the role of a horizontal barrier blocking the free flow of seepage below the surface. It is meant to model what happens if, at that barrier, interstitial voids between sand grains are filled, creating a cohesive stratum as Figure 7 suggests. Effects of seepage on mass transfer are diminished if such barrier is located at a depth $\ell_i \lesssim L/(2\pi)$. With $\ell_i \sim L/(8\pi)$, the distance from seepage barrier to trough is so small that humidity begins to pass across the trough instead. Figure 11 also shows that it is legitimate to model the ripple as flat (dashed lines) rather than wavy (solid lines), as long as ℓ_i remains small. Such assumption greatly simplifies the theory.

Our excavations at points 12-14 revealed cohesive sands at depths $> L/(2\pi)$, consistent with persistent moisture having relatively low vertical gradients. As the bottom Figure 7 shows, such material lies at > 2 cm beneath the trough, but it does not rise to the surface, except as vertical fingers of cohesive material reaching just beneath crests. Although this pattern may be attributed to fingering observed after much liquid water penetrates sand [Parlange, 1980; Nieber, 1996; Dekker and Ritsema, 1994; Ritsema et al., 1998], it also resembles the channeling predicted by the model and illustrated in Figure 9.

In short, our advection-diffusion model predicts that, with seepage, ripple troughs adopt ambient conditions more readily. Crests, on the other hand, are where moisture is channeled, mainly in the vertical direction, thus likely building greater cohesion within accretions shaped like the theoretical contours of Ω in Figure 9.

4.2. Dust filtration

Seepage causes small particles to penetrate ripples through interstices between sand grains. In Appendix B, we calculate how a monodisperse dust accumulates in the bed. We show that the evolution of dust concentration along seepage streamlines of relative curvilinear coordinate

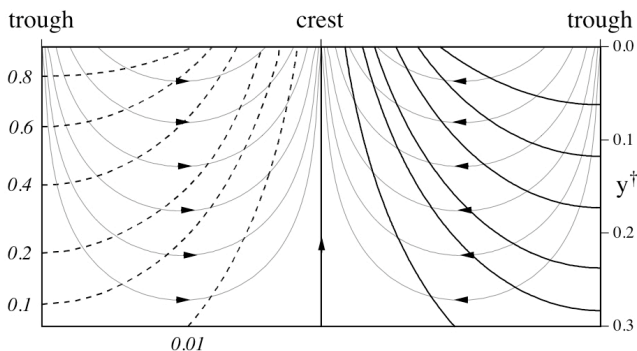


Figure 12. Contours of relative dust concentration \bar{n}° within the bed (dashed and solid lines) and seepage streamlines (thin lines with arrows) along a ripple wavelength from trough to trough and along y^\dagger for $M^\dagger \simeq 925$, $L^\dagger \simeq 0.40$, without a seepage barrier. Values of \bar{n}° for each contour are shown in italics outside the left graph. Solid lines on the right graph are from the numerical integration of equation (8) with varying $\text{Sh}(s^\dagger)$; dashed lines on the left are from the simpler closed-form expression of equation (B13) with $\text{Sh} = \text{Sh}_{\text{FD}} = \text{Sh}_\infty$, such that $\Gamma_d^\dagger \simeq 2.9$. Seepage streamlines are described by $y^\dagger = [1/(2\pi)] \ln[\sin(2\pi x^\dagger)/\sin(2\pi x_0^\dagger)]$.

$s^\dagger = [1/(2\pi)] \ln[\tan(\pi x^\dagger)/\tan(\pi x_0^\dagger)]$ is governed by

$$\frac{1}{\bar{n}^\circ} \frac{\partial \bar{n}^\circ}{\partial s^\dagger} = -\Gamma_d^\dagger \frac{[1 + \tan^2(\pi x_0^\dagger)] \exp(2\pi s^\dagger)}{[1 + \tan^2(\pi x_0^\dagger)] \exp(4\pi s^\dagger)}, \quad (5)$$

where $0 \leq x_0^\dagger \leq 1/4$ is the relative abscissa at which the flow penetrates the surface, $\bar{n}^\circ \equiv \bar{n}/n_0$ is the number density of dust relative to its value n_0 in the ambient, and Γ_d^\dagger is a local dimensionless volumetric rate of dust deposition. (The number density n of monodisperse spherical dust grains of diameter d_b and mass $m_b = (\pi/6)d_b^3\rho_b$ is related to their mass concentration $C_b = nm_b$). As Figure ?? illustrates, dust accumulates beneath troughs (but not beneath crests), and reaches depths that exceed the characteristic length $L/2\pi$ of seepage. Because Brownian diffusion is slow, such accumulation would not take place without ripple-induced seepage. (Appendix B3 calculates that, without seepage, dust cannot infiltrate the bed). In short, ripples act as a filter of fine particles. Huettel et al. [2007] made similar observations with underwater ripples.

In the companion paper, we showed that the reptation layer collapses more readily above ripple troughs than crests, that crests are made up of loose and mobile granular material, while troughs uncover a longer-lasting, densely packed surface [Louge et al., 2009], and that troughs experience a lower surface turbulent shear stress τ_0 than crests at the same wind speed. From the data of Gong et al. [1996], we inferred

$$\tau_0 \simeq 0.0015\rho U^2 \left[1 + \left(\frac{h_0}{L} \right) f(x/L) \right], \quad (6)$$

where f is a function with maximum of +60 at the crest and minimum of -12 at the trough. Therefore, grains held in the troughs do not mobilize easily for two reasons: first, their higher compaction raises the threshold shear stress at which they begin to move; second, even if this threshold is independent of compaction, equation (6) would predict that a typical ripple with $h_0/L = 0.02$ requires a wind speed 70% larger to mobilize sand trapped in a trough [Louge et al., 2009b]. Therefore, any dust stored below troughs can only resuspend at winds that are violent enough to mobilize deeply the relatively compact surface on which the looser ripple crests travel. (Such dust resuspension may be discerned in a video clip available online with our companion paper [Louge et al., 2009]; the movie shows sand ejection and subsequent dust release from ripple troughs upon ramming a foot through a relatively soft dune). Overall, by inducing seepage in the sand bed, ripples draw and accumulate dust below the surface; by shielding their own troughs, they inhibit dust release until the next catastrophic wind event.

5. Conclusions

Stratigraphic measurements near the surface of a barchan sand dune indicated that moisture accumulates mainly below its windward toe. A model of the internal seepage flow driven by variations of static pressure on the surface of a wind-swept ripple predicted that water vapor is channeled through crests, in agreement with excavations below stable ripples that exposed vertical channels of cohesive material beneath these. The model also predicted that mass transfer varies on a depth scale that is a fraction of the ripple wavelength. Finally, our theory implied that small Brownian dust particles accumulate deep beneath ripple troughs and are only resuspended when the relatively more compact sand base is swept away by high winds. Such accumulation would not happen without ripple-induced seepage.

Appendix A: Seepage

Wind blowing on sand ripples creates streamwise variations of the static pressure p on the surface, which in turn drive a “seepage” flow through the porous sand bed. *Gong et al.* [1996] observed that, on a wavy surface,

$$p \simeq p_a + p_0 \cos(2\pi x^\dagger), \quad (\text{A1})$$

where p_a is the ambient pressure, and daggers[†] represent lengths relative to the ripple wavelength L . In their experiments, the pressure amplitude was approximately

$$p_0 \approx \rho U^2 h_0 / (\eta L), \quad (\text{A2})$$

where ρ is gas density, U is wind speed, h_0 is the ripple amplitude, and $\eta \simeq 0.14$. (*Gong et al.* [1996] measured $U \approx 10\text{m/s}$ at $Y \approx 1\text{m}$ above their wavy surface). For a homogeneous porous medium with permeability

$$K \simeq \frac{d^2}{150} \frac{(1-\nu)^3}{\nu^2}, \quad (\text{A3})$$

the viscous Ergun’s equation yields the superficial velocity vector

$$\mathbf{u} = -(K/\mu)\nabla p \quad (\text{A4})$$

in terms of the pressure gradient ∇p and the gas viscosity μ . Steady mass conservation $\nabla \cdot \rho \mathbf{u} = 0$ then reduces to the Laplace equation $\nabla^2 p = 0$. Assuming for simplicity that the surface is flat ($h_0 \ll L$), the solution satisfying equation (A1) at the surface is, for a bottomless bed,

$$\nabla p = -2\pi \frac{p_0}{L} \exp(-2\pi y^\dagger) \{ \sin(2\pi x^\dagger) \hat{\mathbf{x}} + \cos(2\pi x^\dagger) \hat{\mathbf{y}} \}, \quad (\text{A5})$$

yielding the dimensionless velocity field [*Louge et al.*, 2009]

$$\mathbf{u}^\dagger \equiv \mathbf{u} L \mu / (2\pi p_0 K) = \exp(-2\pi y^\dagger) [\sin(2\pi x^\dagger) \hat{\mathbf{x}} + \cos(2\pi x^\dagger) \hat{\mathbf{y}}]. \quad (\text{A6})$$

In the vertical direction, this flow field then decays on the length scale $L/(2\pi)$.

Seepage may be affected by the presence of a flat horizontal barrier beneath the bed at a depth $y = \ell_i$, and through which no seepage can flow ($\mathbf{u} \cdot \hat{\mathbf{y}} = 0$). In this case,

$$p = p_a + p_0 \cos(2\pi x^\dagger) \times \left[\frac{\exp[2\pi(2\ell_i^\dagger - y^\dagger)] + \exp[2\pi y^\dagger]}{1 + \exp(4\pi\ell_i^\dagger)} \right]. \quad (\text{A7})$$

and

$$\mathbf{u}^\dagger = \frac{\exp(2\pi y^\dagger)}{1 + \exp(4\pi\ell_i^\dagger)} \left[\{ \exp[4\pi(\ell_i^\dagger - y^\dagger)] + 1 \} \times \sin(2\pi x^\dagger) \hat{\mathbf{x}} + \{ \exp[4\pi(\ell_i^\dagger - y^\dagger)] - 1 \} \cos(2\pi x^\dagger) \hat{\mathbf{y}} \right], \quad (\text{A8})$$

The left Figure 11 illustrates how the barrier affects the seepage superficial velocity breaking through the surface. It also contrasts the analytical solution of equation (A7) for a flat bed surface at $y^\dagger = 0$ (dashed lines) with a COMSOL MULTIPHYSICS numerical solution of the same equations for a wavy surface geometry. The barrier is hardly felt if it lies at a depth $\ell_i > L$. As it approaches the surface, seepage velocity decreases by the factor $[\exp(4\pi\ell_i^\dagger) - 1] / [\exp(4\pi\ell_i^\dagger) + 1]$. The role of wavy geometry is evident in the asymmetry that numerical curves develop (solid lines) and in their departure from the analytical solution. However, for $h_0/L = 0.02$, such departure is insignificant unless $\ell_i \lesssim L/(2\pi)$, which justifies our simplifying assumption of bed flatness leading to equations (A5)-(A6).

Appendix B: Dust capture

We consider spherical dust grains of diameter d_b and material density ρ_b subject to Brownian diffusivity $D_b = k_b T_a / (3\pi\mu d_b)$, where $k_b \simeq 1.3810^{-23} \text{ J}^\circ\text{K}$ is Boltzmann’s constant and T_a is the absolute ambient temperature. For simplicity, we assume that the sand bed is flat with uniform solid volume fraction $\nu_c \simeq 0.64$. We model it as a network of cylindrical pores of radius $R_p \gg d_b$ aligned with seepage streamlines. The radial velocity profile in the pore is a fully-developed Poiseuille flow with $v = 2\bar{v}(1-r^{\circ 2})$, where \bar{v} is the cross-sectional average interstitial velocity and $r^\circ \equiv r/R_p$ is the dimensionless radial coordinate in the pore. We evaluate

$$R_p/d = (2/5\sqrt{3})(1-\nu_c)/\nu_c \quad (\text{B1})$$

by matching the pressure gradient $|\nabla p| = 8\mu\bar{v}/R_p^2$ that this flow generates with the prescriptions of Ergun’s equations (A3) and (A4). For $d = 200\mu\text{m}$, pores have an effective diameter of $52\mu\text{m}$, large enough to let dust grains through.

B1. Deposition on a single pore

Dust is convected along a single pore by seepage, and diffused radially across it by Brownian motion. We ignore electrostatics and assume that dust particles reaching the wall adhere to it instantly by van der Waals attraction. The balance of their number density is, in dimensionless form,

$$(1-r^{\circ 2}) \frac{\partial n^\circ}{\partial s^\circ} = \frac{1}{r^\circ} \frac{\partial}{\partial r^\circ} \left(r^\circ \frac{\partial n^\circ}{\partial r^\circ} \right), \quad (\text{B2})$$

where the dimensionless coordinate along the pore is $s^\circ \equiv s D_b / (2\bar{v} R_p)$. At the pore wall, the Brownian diffusion flux is equal to the rate Ξ at which particles with Maxwellian fluctuation velocity distribution impact the surface [*Louge*, 1994]. At low dust volume fraction,

$$\Xi = \frac{3}{\pi} \left(\frac{k_b T_a}{\rho_b d_b^3} \right)^{1/2} n_w = -D_b \frac{\partial n}{\partial r} \Big|_{r=R_p}, \quad (\text{B3})$$

where n_w is the wall concentration. In dimensionless form, this surface boundary condition at $r^\circ = 1$ becomes

$$\partial n^\circ / \partial r^\circ = -M^\circ n^\circ, \quad (\text{B4})$$

where $M^\circ \equiv 9\mu R_p / (\rho_b d_b k_b T_a)^{1/2}$. At the pore centerline, $r^\circ = 0$, symmetry dictates

$$\partial n^\circ / \partial r^\circ = 0. \quad (\text{B5})$$

Initially, the relative dust number density at the pore’s entrance on the trough surface, $s^\circ = 0$, is

$$n^\circ = 1. \quad (\text{B6})$$

Because this linear problem is similar to Nusselt’s treatment of convective thermal entry in a cylinder, it is convenient to define the mass transfer coefficient h_b relating wall flux to the difference between the wall and bulk concentrations,

$$-\Xi \equiv h_b (n_w - \bar{n}), \quad (\text{B7})$$

where \bar{n} is the mixed-mean concentration given by

$$\pi R_p^2 \bar{v} \bar{n} \equiv \int_{r=0}^{R_p} v n 2\pi r dr. \quad (\text{B8})$$

Equations (B3) and (B7) yield the Sherwood number

$$\text{Sh} \equiv \frac{h_b R_p}{D_b} = \frac{1}{(n_w^\circ - \bar{n}^\circ)} \frac{\partial n^\circ}{\partial r^\circ}. \quad (\text{B9})$$

This problem has two asymptotic limits depending on whether dust capture is limited by a slow Brownian diffusion ($M^\circ \rightarrow \infty$), in which case $n_w \rightarrow 0$, or whether the diffusion is vigorous ($M^\circ \rightarrow 0$). The latter case is equivalent to the Nusselt problem with constant wall flux, while the former resembles his problem with constant wall temperature. In either case, PDE (B2) subject to boundary conditions (B4) and (B5) and to initial condition (B6) has a series solution readily obtained by separation of variables. A fully-developed solution, for which h_b is constant, is reached as soon as $s^\circ \gtrsim 0.1$. In that case, we calculate that the fully-developed Sherwood number is conveniently approximated by the expression $\text{Sh}_{\text{FD}} \simeq \text{Sh}_0 - (\text{Sh}_0 - \text{Sh}_\infty)[1 - \exp(-4.9M^{0.14})]^{1.46}$, where $\text{Sh}_0 = 24/11$ is the classical result of the fully-developed Nusselt problem with constant wall heat flux, and $\text{Sh}_\infty \simeq 1.83$ is its counterpart with constant wall temperature. In general, for fully-developed diffusion of dust, equations (B3), (B7) and (B9) yield the following relation between wall and bulk dust concentrations:

$$\frac{n_w}{\bar{n}} = \frac{1}{(1 + M^\circ/\text{Sh})}. \quad (\text{B10})$$

B2. Volumetric dust capture

We use the above analysis for a single pore to estimate the local volumetric rate Γ_d of dust deposition in the bed. If, for simplicity, pores form a network of equally-spaced curvilinear cylinders, their separation ℓ_d satisfies $\ell_d/R_p = \sqrt{\pi/(1-\nu_c)}$. Then, equations (B7) and (B10) yield

$$\Gamma_d = \left(\frac{2}{3\pi}\right) \left(\frac{k_b T_a}{\mu d_b R_p^2}\right) \frac{(1-\nu_c)\bar{n}}{(1/M^\circ) + (1/\text{Sh})}. \quad (\text{B11})$$

The dust concentration balance within the bed includes terms for seepage convection, bulk diffusion, and volumetric deposition rate. In dimensionless form, they are

$$\mathbf{u}^\dagger \cdot \nabla \bar{n}^\circ = D_b^\dagger \nabla^2 \bar{n}^\circ - \Gamma_d^\dagger \bar{n}^\circ, \quad (\text{B12})$$

where \mathbf{u}^\dagger is given by equation (A6),

$$D_b^\dagger \equiv \left(\frac{25}{\pi^2}\right) \left(\frac{k_b T_a}{p_0 d^2 d_b}\right) \left(\frac{\nu_c}{1-\nu_c}\right)^2,$$

and $\Gamma_d^\dagger \equiv (4L^\circ)[M^{\circ-1} + \text{Sh}^{-1}]^{-1}$. The quantity

$$L^\circ \equiv \frac{s^\circ}{s^\dagger} \equiv \left(\frac{1875}{8\pi^2}\right) \left(\frac{L}{d}\right)^2 \left(\frac{k_b T_a}{d^2 d_b p_0}\right) \left(\frac{\nu_c}{1-\nu_c}\right)^4$$

is the ripple wavelength expressed in the dimensionless scale along the pore. If pores have reached fully-developed deposition in dusty air at $T_a = 300^\circ\text{K}$, $U = 10$ m/s, laden with $2\mu\text{m}$ particles with $\rho_d = \rho_s = 2500\text{kg/m}^3$, in a sand bed of $200\mu\text{m}$ grains with ripples of 0.15m wavelength, then $M^\circ \simeq 925 \gg 1$, $\text{Sh}_{\text{FD}} \simeq \text{Sh}_\infty$, $L^\circ \simeq 0.40$, $D_b^\dagger \simeq 210^{-8} \ll 1$, and $\Gamma_d^\dagger \simeq 2.9$. Therefore, dust deposition within the pores is diffusion-limited, and the bulk diffusion term in equation (B12) can be ignored. Consequently, it is legitimate to view dust deposition as occurring in individual pores that are aligned with seepage streamlines, but that are not interconnected with other pores by lateral diffusion.

In this case, the evolution of the concentration profiles along streamlines is subject to an equation that is simpler than equation (B12). To establish it, we project the superficial velocity in equation (A6) on the streamline of unit vector $\hat{\mathbf{s}}$, $\mathbf{u}^\dagger \cdot \hat{\mathbf{s}} = \exp(-2\pi y^\dagger)$, eliminate $\exp(2\pi y^\dagger)$ in terms of s^\dagger and x_0^\dagger , and obtain equation (8). Because in general the

Sherwood number in equation (B9) depends on s^\dagger as deposition develops along the flow, we first calculate $\text{Sh} = \text{Sh}(s^\dagger)$ from equations (B2), (B4)-(B6) and (B9) using MATLAB's pdepe routine, and then we integrate ODE (8) numerically subject to $\bar{n}^\circ = 1$ at the trough surface ($s^\dagger = 0$ or $x^\dagger = x_0^\dagger$). If instead we assume, more simply, that deposition is fully-developed right from the surface, equation (8) has the analytical solution

$$\bar{n}^\circ = \exp\left[-\Gamma_d^\dagger \frac{(x^\dagger - x_0^\dagger)}{\sin(2\pi x_0^\dagger)}\right]. \quad (\text{B13})$$

Dust penetrates the trough where $0 \leq x_0^\dagger < 1/4$ (or $3/4 \leq x_0^\dagger < 1$) and $\bar{n} = \bar{n}_0$. A smaller fraction of its population emerges around the crest, where $1/4 < x^\dagger < 3/4$, $\bar{n} \ll \bar{n}_0$ and deposition is nearly fully-developed. Thus, the net dust flow rate crossing the ripple surface on a whole wavelength in a unit time and unit ripple width is

$$Q = \left(\frac{p_0 d^2}{75\mu}\right) \frac{(1-\nu_c)^3}{\nu_c^2} \bar{n}_0 (1 - \mathcal{I}). \quad (\text{B14})$$

\mathcal{I} is the integral contribution of dust emerging around the crest at x^\dagger , which originated at $x_0^\dagger = 1/2 - x^\dagger$. Using equation (B13),

$$\mathcal{I} = 2\pi \int_{1/4}^{1/2} \cos(2\pi x^\dagger) \exp\left[-\Gamma_d^\dagger \frac{(2x^\dagger - 1/2)}{\sin(2\pi x^\dagger)}\right] dx^\dagger. \quad (\text{B15})$$

Its numerical integration is closely fit by the expression $\mathcal{I} \simeq [1 - \exp(-8.36/\Gamma_d^{\dagger 0.075})]^{3200}$.

Dust accumulation can eventually plug pores at the trough surface, thus blocking further penetration below. Assuming that dust adheres to pore walls at the random loose packing ν_m , and that bed permeability does not change, the rate of shrinkage of the pore radius is given by

$$dR_p/dt = -(\pi d_b^3)/(6\nu_m)\Xi. \quad (\text{B16})$$

Because dust deposition is diffusion-limited ($M^\dagger \rightarrow \infty$), equations (B1), (B7), (B10) and (B16) yield $[1 - (R/R_p)^2] = t/t_\infty$, where

$$t_\infty = \frac{12}{25} \left(\frac{\mu}{k_b T_a \bar{n}_0}\right) \left(\frac{d}{d_b}\right)^2 \left(\frac{1-\nu_c}{\nu_c}\right)^2 \left(\frac{\nu_m}{\text{Sh}_\infty}\right)$$

is an estimate of the (typically very long) time to plug a pore at the trough surface based on fully-developed dust deposition.

B3. No capture without seepage

Without seepage, dust cannot infiltrate the sand bed by Brownian diffusion alone. Assuming vertical pores without net flow, equation (B2) is replaced by

$$\frac{\partial^2 n^\circ}{\partial y^{\circ 2}} + \frac{1}{r^\circ} \frac{\partial}{\partial r^\circ} \left(r^\circ \frac{\partial n^\circ}{\partial r^\circ}\right) = 0, \quad (\text{B17})$$

where $y^\circ \equiv y/R_p$. With the boundary conditions (B4) and (B5) and $n^\circ = 1$ at the surface ($y^\circ = 0$), the solution, once integrated radially in a pore, yields the average relative dust concentration

$$\bar{n}^\circ = 2 \sum_{i=1}^{\infty} \exp(-\lambda_i y^\circ) \left[\int_0^1 J_0(\lambda_i r^\circ) r^\circ dr^\circ \right]^2 / \left[\int_0^1 J_0^2(\lambda_i r^\circ) r^\circ dr^\circ \right], \quad (\text{B18})$$

where λ_i are eigenvalues solution of $\lambda_i J_1(\lambda_i) = M^\circ J_0(\lambda_i)$, and J_0 and J_1 are Bessel functions of the first kind with order zero and one, respectively. For typical $M^\circ \gg 1$, the first term in series (B17) dominates, and the characteristic ($1/e$) penetration depth is $y \simeq R_p/\lambda_1$. This infiltration distance ($11\mu\text{m}$ for $200\mu\text{m}$ sand grains with $M^\circ = 925$ and $\lambda_1 \simeq 2.4$) is much shallower than that achieved with seepage. In short, fine particles can only penetrate the surface if assisted by seepage.

Acknowledgments. Louge developed the theory, and conceived instrumentation and experiments, which he conducted in Mauritania with Ould el-Moctar, Valance, and Ould Ahmedou. Moreau-Trouvé and Mint Babah measured dielectric sand properties at the laboratory in Rennes. The authors gratefully acknowledge fruitful conversations with Simon Bercovicz, Daniel Beyssens, Marco Bittelli, Joseph Calantoni, Lance Collins, Robert B. Haehnel, Anthony G. Hay, Philip T. Metzger, Jean-Yves Parlange, Renee E. Richer, Benoit R. Roisin, Tammo Steenhuis, and Robert J. Sullivan. They are indebted to Robert L. Foster for loaning the stratigraphic probe and sharing his expertise, to Ahmedou Ould Mahfoudh for his support in the field, and to Patrick Chasles, Stéphane Bourlès, Hervé Orain and Mikäel Fontaine for technical help with instruments. This work was funded by the “Ministère de la Recherche” and “Agence Nationale de la Recherche” under grants ACI-500270 and ANR-05-BLAN-0273. MYL’s travel was supported by NSF grant INT-0233212.

References

- Andreotti, B. (2004), A two-species model of aeolian sand transport, *J. Fluid Mech.*, *510*, 47–70.
- Andreotti, B., P. Claudin, and S. Douady (2002), Selection of dune shapes and velocities part 1: Dynamics of sand, wind and barchans, *Eur. Phys. J. B*, *28*, 321–339.
- Andreotti, B., P. Claudin, and O. Pouliquen (2006), Aeolian sand ripples: Experimental study of fully developed states, *Phys. Rev. Lett.*, *96*, 028,001.
- Andreotti, B., P. Claudin, and O. Pouliquen (2008), Measurements of the aeolian sand transport saturation length, *arXiv:cond-mat*, *0806.3931v1*, 1–5.
- Bagnold, R. (1935), The movement of desert sand, *The Geographical J.*, *85*, 342–365.
- Böttcher, C. (Ed.) (1952), *Theory of Electric Polarization*, Elsevier, New York.
- Bristow, C., S. Bailey, and N. Lancaster (2000), The sedimentary structure of linear sand dunes, *Nature*, *406*, 56–59.
- Carslaw, H. S., and J. C. Jaeger (1959), *Conduction of heat in solids, second edition*, Clarendon Press, Oxford, chapter 2.
- Cook, P. L. M., F. Wenzhöfer, R. N. Glud, F. Janssen, and M. Huettel (2007), Benthic solute exchange and carbon mineralization in two shallow subtidal sandy sediments: Effect of advective pore-water exchange, *Limnol. Oceanogr.*, *52*, 1943–1963.
- Csahók, Z., C. Misbah, F. Rioual, and A. Valance (2000), Dynamics of aeolian sand ripples, *Eur. Phys. J. E*, *3*, 71–86.
- Dekker, L. W., and C. J. Ritsema (1994), Fingering flow: the creator of sand columns in dune and beach sands, *Earth Surf. Proc. and Landforms*, *19*, 153–164.
- Gong, W., P. A. Taylor, and A. Dörnbrack (1996), Turbulent boundary-layer flow over fixed aerodynamically rough two-dimensional sinusoidal wave, *J. Fluid Mech.*, *312*, 1–31.
- Hersen, P. (2004), On the crescentic shape of barchan dunes, *Eur. Phys. J. B*, *37*, 507–514.
- Huettel, M., P. L. M. Cook, F. Janssen, G. Lavik, and J. J. Middelburg (2007), Transport and degradation of a dinoflagellate bloom in permeable sublittoral sediment, *Mar. Ecol. Prog. Ser.*, *340*, 139–153.
- Livingstone, I., G. F. Wiggs, and C. M. Weaver (2007), Geomorphology of desert sand dunes: A review of recent progress, *Earth-Science Rev.*, *80*, 239–257.
- Louge, M. Y., A. Valance, A. Ould el-Moctar, and P. Dupont (2009), Packing variations on a ripple of nearly monodisperse dry sand, *J. Geophys. Res.*, in press.
- Louge, M. Y., A. Valance, A. Ould el-Moctar, D. Ould Ahmedou, and P. Dupont (2009b), Model for surface packing and aeolian transport on sand ripples, in: *Powders and Grains 2009*, pp. 951–954, Nakagawa, M. and Luding, S., eds., American Institute of Physics, Melville, NY, AIP Conference Proceedings 1145.
- Louge, M. Y. (1994), Computer simulations of rapid granular flows of spheres interacting with a flat, frictional boundary, *Phys. Fluids*, *6*, 2253–2269.
- Louge, M. Y., R. Steiner, S. C. Keast, R. Decker, J. Dent, and M. Schneebeli (1997), Application of capacitance instrumentation to the measurement of density and velocity of flowing snow, *Cold Regions Sci. and Technol.*, *25*, 47–63.
- Louge, M. Y., R. L. Foster, N. Jensen, and R. Patterson (1998), A portable capacitance snow sounding instrument, *Cold Regions Sci. and Technol.*, *28*, 73–81.
- Manukyan, E., and L. Prigozhin (2009), Formation of aeolian ripples and sand sorting, *Phys. Rev. E*, *79*, 031303.
- Maxwell, J. C. (1892), *Electricity and Magnetism, Vol. 1*, Clarendon, Oxford.
- McKee, E. D. (Ed.) (1979), *A Study of Global Sand Seas*, Geological Survey Professional Paper 1052, US Department of the Interior and NASA, United States Government Printing Office, Washington, DC.
- Meysman, F. J. R., O. S. Galaktionov, P. L. M. Cook, F. Janssen, and M. Huettel (2007), Quantifying biologically and physically induced flow and tracer dynamics in permeable sediments, *Biogeosciences*, *4*, 627–646.
- Nieber, J. L. (1996), Modeling finger development and persistence in initially dry porous media, *Geoderma*, *70*, 207–229.
- Ould Ahmedou, D., A. Ould Mahfoudh, A., Dupont, P., Ould el-Moctar, A., Valance, A., and Rasmussen, K. R. (2007), Barchan dune mobility in Mauritania related to dune and interdune sand fluxes, *J. Geophys. Res.*, *112*, F02016:1–18.
- Parlange, J.-Y. (1980), Water transport in soils, *Ann. Rev. Fluid Mech.*, *12*, 77–102.
- Parsons, D. R., G. F. Wiggs, I. J. Walker, R. I. Ferguson, and B. G. Garvey (2004), Numerical modelling of airflow over an idealised transverse dune, *Environmental Modelling & Software*, *19*, 153–162.
- Rasmussen, K. R., J. D. Iversen, and P. Rautahemio (1996), Saltation and wind-flow interaction in a variable slope wind tunnel, *Geomorphology*, *17*, 19–28.
- Ritsema, C. J., L. W. Dekker, J. L. Nieber, and T. Steenhuis (1998), Modeling and field evidence of finger formation and finger recurrence in a water repellent sandy soil, *Water Resources Research*, *34*, 555–567.
- Sauermaann, G., K. Kroy, and H. J. Herrmann (2001), Continuum saltation model for sand dunes, *Phys. Rev. E*, *64*, 031,305.
- Schwämmle, V., and H. Herrmann (2005), A model of barchan dunes including lateral shear stress, *Eur. Phys. J. E*, *16*, 57–65.
- Torquato, S. (1995), Nearest-neighbor statistics for packings of hard spheres and disks, *Phys. Rev. E*, *51*, 3170–3182.
- Wiggs, G., I. Livingstone, and A. Warren (1996), The role of streamline curvature in sand dune dynamics: Evidence from field and wind tunnel measurements, *Geomorphology*, *17*, 29–46.
- M. Y. Louge, Sibley School of Mechanical and Aerospace Engineering, Cornell University, Ithaca, NY 14853, USA. (MYL3@cornell.edu)
- A. Valance, Institut de Physique de Rennes, CNRS UMR 6251, Université de Rennes 1, Campus Beaulieu, Bat 11A, 35042 Rennes Cédex, France. (alexandre.valance@univ-rennes1.fr)
- H. Mint Babah, Université de Rennes 1, France. (houda.mintbabah@univ-rennes1.fr)
- J.-C. Moreau-Trouvé, Lycée Victor Hugo, 26 avenue François Mitterrand, 56700 Hennebont, France. (jean-charles.moreau-trouve@ac-rennes.fr)
- A. Ould el-Moctar, Ecole Polytechnique de l’Université de Nantes, Laboratoire de Thermocinétique, UMR CNRS 6607, 44306 Nantes Cédex 3, France. (ahmed.ouldelmoctar@univ-nantes.fr)
- P. Dupont, Institut National des Sciences Appliquées de Rennes, 20, Avenue des Buttes de Coësmes, 35043 Rennes Cédex, France. (Pascal.Dupont@insa-rennes.fr)
- D. Ould Ahmedou, Faculté des Sciences, Université de Nouakchott, République Islamique de Mauritanie. (dah@univ-nkc.mr)